Chinese Chemical Letters 37 (2026) 111425

Contents lists available at ScienceDirect

Chinese Chemical Letters

journal homepage: www.elsevier.com/locate/cclet

# Halogen-bonded organic frameworks (XOFs) based on [N···Br$^+$···N] bonds for enhanced photothermal cancer therapy

Siyi Lin[a,1], Qingxue Xu[b,1], Xuguan Bai[a,1], Zhennan Tian[a], Lu Wang[a], Fuxin Han[c,*], Shigui Chen[a,*], Qiang Cai[b,*]

[a] The Institute for Advanced Studies, Hubei Key Lab on Organic and Polymeric Opto-Electronic Materials, Wuhan University, Wuhan 430072, China
[b] Department of Neurosurgery, Renmin Hospital of Wuhan University, Wuhan University, Wuhan 430060, China
[c] Neurological intensive care unit, Second Affiliated Hospital of Shaanxi University of Chinese Medicine, Xianyang 712000, China

ARTICLE INFO

*Article history:*
Received 19 February 2025
Revised 12 May 2025
Accepted 6 June 2025
Available online 7 June 2025

*Keywords:*
[N···Br$^+$···N] halogen bond
Supramolecular medicine
Photothermal therapy
Tumor treatment

ABSTRACT

Effective treatment of subcutaneous tumors remains a focal point in cancer therapy. Photothermal therapy, a novel therapeutic approach, has emerged as a promising alternative, offering a less invasive option for the treatment of subcutaneous tumors. This study reports the exploration of novel supramolecular halogen-bonded organic frameworks (XOFs) based on [N···Br$^+$···N] halogen bonds through the ligand exchange strategy and their application in photothermal therapy. Through ligand exchange, XOF(Br)-TPy was successfully prepared, and its structure and properties were thoroughly characterized using NMR, XPS, FT-IR, and XRD techniques. Due to their cationic characteristics, these XOFs serve as effective carriers for the photothermal agent IR820. *In vitro* experiments demonstrated that the IR820@XOF(Br)-TPy composite exhibits excellent photothermal conversion efficiency under NIR irradiation, effectively inducing tumor cell ablation. Furthermore, *in vivo* studies confirmed the remarkable antitumor efficacy of the composite material in a subcutaneous tumor model. This work demonstrates that the ligand exchange strategy is a versatile and facile approach for constructing XOFs(Br) and provides a novel strategy for developing advanced photothermal therapeutic agents with significant application potential.

© 2025 Published by Elsevier B.V. on behalf of Chinese Chemical Society and Institute of Materia Medica, Chinese Academy of Medical Sciences.

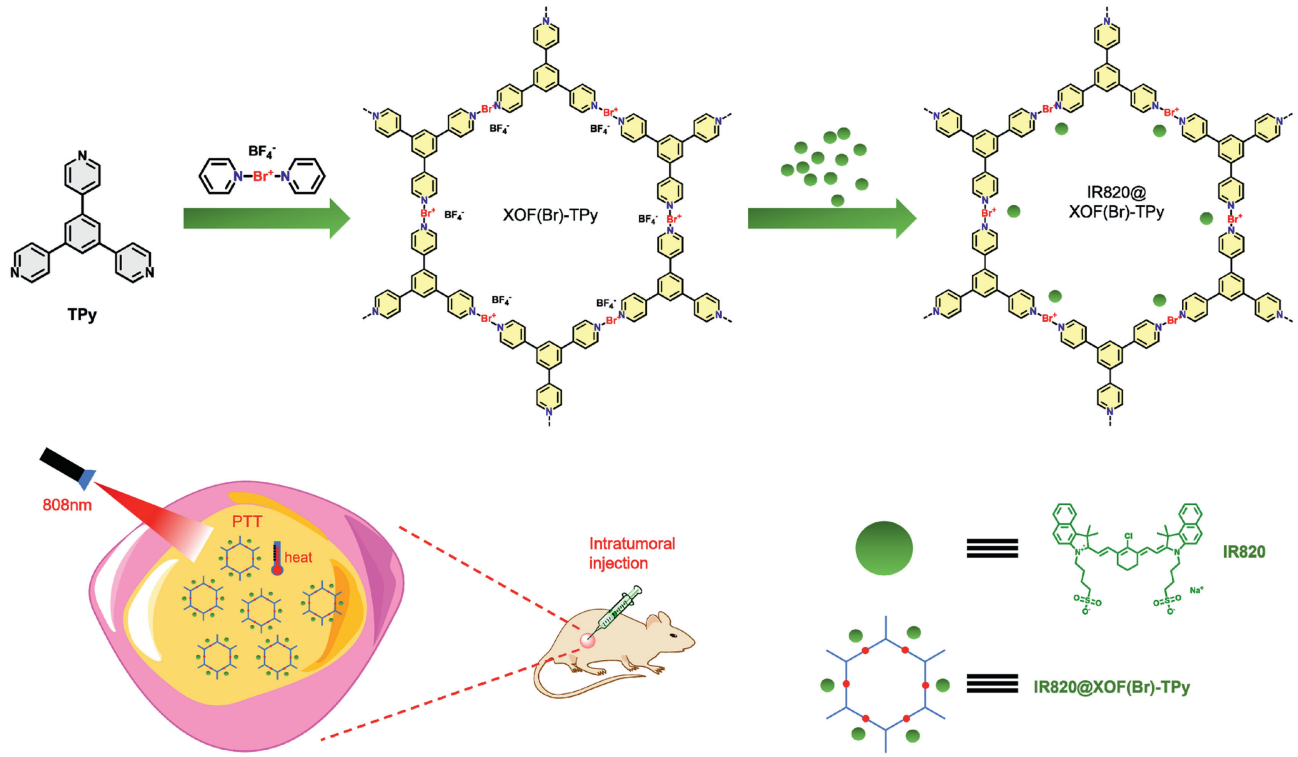
Cancer poses a significant threat to human health [1] and necessitates the urgent development of effective therapeutic strategies [2–4]. However, achieving effective cancer treatment remains an ongoing challenge. Traditional cancer therapies, including chemotherapy [5], radiotherapy [6,7], and surgery [8], might lead to significant trauma, irreversible organ damage or local tissue fibrosis. As a result, minimally invasive medical technologies [9,10] have garnered substantial research interest as a means to overcome these limitations. Among these, photothermal therapy (PTT) has emerged as a promising minimally invasive treatment modality [11–13]. In recent years, near-infrared (NIR) laser-responsive PTT [14] has attracted widespread attention due to its non-invasive nature and minimal side effects. PTT utilizes its photothermal mechanism to elevate local temperatures, thereby inducing irreversible damage to tumor cells. The success of photothermal therapy hinges on the development of efficient, biocompatible, and precisely targeted photothermal agents [15].

In recent years, the development of nanomedicines has garnered significant attention. Various nanocarrier systems, including albumin nanoparticles [16], virus or bacteriophage-based nanoparticles [17,18], organic nanoparticles (such as liposomes [19], micelles [20], and polymeric nanoparticles [21–23]), and inorganic porous materials [24], have demonstrated remarkable potential in enhancing the efficacy of therapeutic agents. Among these, cationic materials have attracted considerable interest due to their efficient loading capacity for anionic therapeutic agents through electrostatic interactions [25]. However, the synthesis of these materials is often complex, limiting their practical applications. Therefore, the development of simple and efficient synthetic methods to construct cationic carriers is of great scientific significance and practical value for achieving effective loading of anionic therapeutic agents and optimizing their therapeutic outcomes.

Supramolecular materials self-assemble through various noncovalent interactions, including hydrogen bonding, van der Waals forces, coordination bonds, $\pi$-$\pi$ stacking, and hydrophobic effects, exhibiting tunable properties and multifunctionality [26–29]. Supramolecular drugs have also attracted more and more attention [30]. Among these, supramolecular materials with positive charges demonstrate significant anion loading capacity *via* elec-

* Corresponding authors.
*E-mail addresses:* 93501192@qq.com (F. Han), caiqno@whu.edu.cn (S. Chen), sgchen@whu.edu.cn (Q. Cai).
[1] These authors contributed equally to this work.

https://doi.org/10.1016/j.cclet.2025.111425
1001-8417/© 2025 Published by Elsevier B.V. on behalf of Chinese Chemical Society and Institute of Materia Medica, Chinese Academy of Medical Sciences.




**Scheme 1.** Preparation and biomedical applications of XOF(Br)-TPy and IR820@ XOF(Br)-TPy.

trostatic interactions [31,32], enabling the efficient encapsulation of anionic therapeutics such as nucleic acids, proteins, and small molecule drugs. The electrostatic interactions between the positively charged supramolecular materials and negatively charged therapeutic agents facilitate their efficient loading and controlled release, thereby enhancing their bioavailability and stability [33]. Halogen bonding, a specific type of non-covalent interaction involving the $\sigma$-hole or p-hole of a halogen atom and the lone pair electrons or $\pi$-electrons of a nucleophilic atom [34–36], has emerged as a powerful tool in supramolecular chemistry. Notably, three-center, four-electron halogen bonds, such as [N···$X^+$···N], feature a positively charged halogen atom ($X^+$) interacting with two Lewis bases, exhibiting excellent directionality and stability [37–40]. This interaction imparts a positive charge to the overall molecular structure, making it an ideal platform for the loading of anionic drugs. Due to its unique three-center structure and strong electronic sharing properties, this bonding mode facilitates the construction of various structures, including supramolecular cages [41], capsules [42], macrocyclic complexes [43], and helicases [44]. Halogen-bonded organic frameworks (XOFs) [45–47] based on three-center, four-electron [N···$X^+$···N] halogen bonds [48] have been extensively explored for applications in adsorption [49–51], catalysis [52–55], magnetism [56], bacterial resistance [57] and others [58]. Owing to the intrinsic cationic nature of the halogen-bonded organic framework (XOF), it is anticipated that anionic photothermal agents can be efficiently loaded onto the bromide-based cationic framework through an anion exchange strategy, thereby enabling the treatment of subcutaneous tumors *via* photothermal therapy (PTT). Herein, we report the preparation of supramolecular halogen-bonded organic frameworks based on bromine cations, XOF(Br)-TPy. These frameworks were synthesized *via* a ligand exchange reaction with $Py_2BrBF_4$, forming structures based on [N···$Br^+$···N] interactions. Compared with traditional cation exchange methods for XOF preparation, this ligand exchange approach eliminates the drawback of residual AgBr being difficult to remove while providing a more effective electrostatic interaction platform for loading anionic photothermal agents. This work represents the first successful synthesis of [N···$Br^+$···N]-linked supramolecular halogen-bonded organic frameworks using a ligand exchange strategy. Their successful construction was confirmed by NMR, XPS, and FT-IR, while their crystallinity was validated by XRD and TEM analyses. The biomedical potential of XOF(Br)-TPy was further explored by loading the photothermal agent IR820 onto the framework, as demonstrated by XPS, UV-vis, EDS, and zeta potential measurements. The *in vitro* photothermal performance of IR820@XOF(Br)-TPy was evaluated, revealing superior photothermal properties compared to IR820 or XOF(Br)-TPy alone. Subsequently, *in vitro* cytotoxicity assays under 808 nm laser irradiation demonstrated that IR820@XOF(Br)-TPy effectively inhibited tumor cell growth. To investigate its *in vivo* photothermal therapeutic efficacy, IR820@XOF(Br)-TPy was administered *via* intratumoral injection in a subcutaneous tumor mouse model. *In vivo* experiments, including photothermal measurements, tumor volume monitoring, mouse weight tracking, and histological analysis of tumor slices, revealed that IR820@XOF(Br)-TPy significantly suppressed tumor growth with excellent biocompatibility. These findings highlight the remarkable photothermal therapeutic potential of IR820@XOF(Br)-TPy. This study represents the first successful preparation of [N···$Br^+$···N]-based XOFs using a ligand exchange strategy, providing new insights into the preparation of XOFs. It further demonstrates the advantages of supramolecular halogen-bonded organic frameworks in tumor therapy, highlighting their potential to expand the biomedical applications of XOFs (Scheme 1).

The feasibility of constructing $Br^+$-based XOFs *via* ligand exchange strategy was explored. XOF(Br)-TPy was prepared by reacting $Py_2BrBF_4$ with 1,3,5-tris(4-pyridyl)benzene (TPy). In $Py_2BrBF_4$, the bromonium cation ($Br^+$) serves as the key halogen bond donor. The formation was firstly monitored by $^1$H NMR spectroscopy (Fig. 1a). The formation of the [N···$Br^+$···N] halogen bonds, resulting

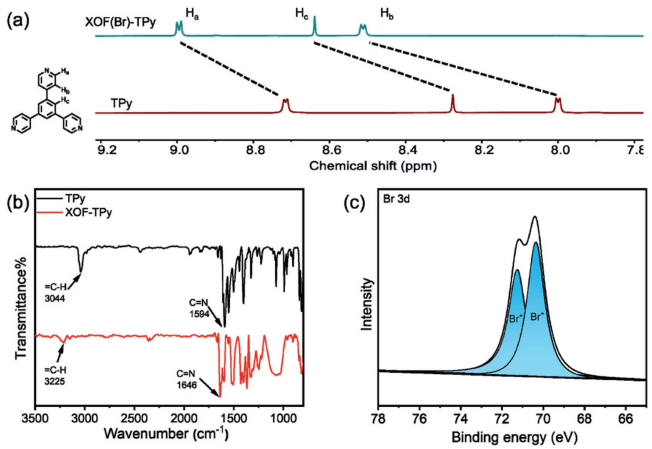



**Fig. 1.** (a) Partial $^1$H NMR spectra of TPy and XOF(Br)-TPy in DMSO-$d_6$ (600 MHz, 298 K). (b) IR spectra of TPy and XOF(Br)-TPy. (c) XPS spectrum of Br 3d for XOF(Br)-TPy.

from ligand exchange, was evidenced by significant perturbations in the magnetic environment of TPy and pyridine. In XOF(Br)-TPy, the $^1$H NMR signals of Ha-Hc experienced distinct downfield shifts compared to free TPy. Specifically, the Ha and Hb pyridyl proton peaks shifted from 8.71 ppm and 8.00 ppm to 9.00 ppm and 8.51 ppm, respectively. These pronounced downfield shifts of the pyridyl protons are attributed to the interaction between $Br^+$ and TPy during the formation of XOF(Br)-TPy. This interaction induces a substantial deshielding effect on the pyridyl groups, reducing their electron density. These observations strongly support the successful construction of XOF(Br)-TPy *via* halogen bond formation between $Br^+$ and TPy.

X-ray photoelectron spectroscopy (XPS) provided detailed surface chemical state analysis of XOF(Br)-TPy (Fig. 1b). In XOF(Br)-TPy, Br 3d peaks were observed at 71.3 eV (Br $3d_{3/2}$) and 70.4 eV (Br $3d_{5/2}$), confirming the presence of $Br^+$. Fourier-transform infrared (FT-IR) spectroscopy (Fig. 1c) revealed significant blue shifts in the C=N stretching vibrations of the pyridyl groups: 52 $cm^{-1}$ for XOF(Br)-TPy. Correspondingly, the =C–H stretching vibrations exhibited pronounced blue shifts of 181 $cm^{-1}$. These blue shifts are consistent with the formation of [N···$Br^+$···N] complexes, which reduce electron density around the pyridyl rings, further supporting the coordination between the pyridyl groups and $Br^+$. Nitrogen gas adsorption isotherms at 77 K were measured to assess the porosity of XOF(Br)-TPy. The Brunauer-Emmett-Teller (BET) surface areas were determined to be 14 $m^2/g$ for XOF(Br)-TPy (Fig. S7 in Supporting information). The relatively low porosity is likely due to the presence of bulky counterions ($BF_4^-$), which may be blocking the pores. Thermogravimetric analysis (TGA) under nitrogen atmosphere (Fig. S8 in Supporting information) demonstrated thermal stability up to approximately 240 °C for XOF(Br)-TPy.

The crystal structure of XOF(Br)-TPy was investigated using powder X-ray diffraction (PXRD) analysis (Figs. 2a and d). Structure elucidation was performed using the Forcite molecular dynamics module within Materials Studio, coupled with Pawley refinement. Overlapping (AA), staggered (AB), and ABC stacking models of XOF(Br)-TPy were constructed and optimized. For XOF(Br)-TPy, the experimental PXRD pattern showed excellent agreement with the simulated pattern of the ABC stacking model (Fig. 2b). Pawley refinement yielded unit cell dimensions of a = 26.12 Å, b = 26.59 Å, c = 10.92 Å, $\alpha = \beta = 90°$, $\gamma = 120°$ (Rwp = 4.29 %, Rp = 3.17 %). A strong diffraction peak corresponding to the (110) plane was observed at $2\theta = 5.17°$ (Fig. 2a). The morphology of XOF(Br)-TPy was investigated using transmission electron microscopy (TEM). High-resolution TEM (HR-TEM) revealed well-defined lattice fringes in XOF(Br)-TPy (Fig. 2c), with measured interplanar spacings of 0.62 nm. Diffraction pattern was obtained *via* Fourier transform of the TEM images. Energy-dispersive X-ray spectroscopy (EDS) elemental mapping confirmed the uniform distribution of C, N, and Br elements within XOF(Br)-TPy (Fig. 2d). To further demonstrate the feasibility of constructing bromine-based halogen-bonded organic frameworks (XOFs) *via* the ligand exchange strategy, we also prepared the pyridyl functionalized tetraphenyl ethylene (TPPE) and its corresponding XOF(Br)-TPPE framework. The detailed characterization data for these materials are provided in Supporting information.

This two-dimensional, positively charged halogen-bonded organic framework, XOF(Br)-TPy, was investigated for its potential to load a negatively charged photothermal agent, IR820, and its subsequent application in subcutaneous tumor treatment.

The preparation of IR820@XOF(Br)-TPy is detailed in Supporting information. X-ray photoelctron spectroscopy (XPS) was used to confirm IR820 loading by observing elemental changes between pristine XOF(Br)-TPy and the IR820@XOF(Br)-TPy composite (Fig. 3a). The appearance of high-intensity peaks corresponding to S 2s, S 2p, and Cl 2p indicated successful loading of IR820. UV-vis absorption spectroscopy further corroborated IR820 loading (Fig. 3b). A broad absorption peak at 690 nm was observed for IR820@XOF(Br)-TPy, suggesting a blue shift from the 750 nm peak of free IR820. Zeta-potential measurements (Fig. 3d) showed a decrease from $28.1 \pm 0.3$ mV for XOF(Br)-TPy to $8.5 \pm 0.3$ mV for IR820@XOF(Br)-TPy, consistent with electrostatic interactions between the cationic XOF(Br)-TPy and anionic IR820. Energy-dispersive X-ray spectroscopy (EDS) elemental mapping (Fig. 3c) confirmed the uniform distribution of S and Cl (characteristic elements of IR820), further demonstrating successful IR820 loading. The photothermal performance of IR820@XOF(Br)-TPy was evaluated by monitoring temperature changes under 808 nm laser irradiation (Figs. 3e and f). Pure water, XOF(Br)-TPy, and free IR820 (at the same concentration as in the composite) served as controls. The IR820@XOF(Br)-TPy solution exhibited rapid heating, reaching 47 °C from an initial 22 °C within 360 s. In contrast, the temperature of the water control remained unchanged, and the free IR820 solution only reached 38 °C. Thermographic images visually confirmed the superior photothermal performance of IR820@XOF(Br)-TPy compared to free IR820. This enhanced performance is likely attributable to the improved dispersion and near-infrared light absorption efficiency of IR820 when loaded onto XOF(Br)-TPy, leading to more efficient photothermal conversion.

Motivated by the excellent photothermal properties of IR820@XOF(Br)-TPy, its anticancer effect was investigated *in vitro* using Glioma cell lines (U87 cancer cells). Compared to the commonly used iodonium cations ($I^+$) in previous studies, $Br^+$ exhibits stronger oxidative properties, which may enhance its ability to kill tumor cells and thus improve therapeutic efficacy. A CCK-8 assay was used to assess cell viability of IR820@XOF(Br)-TPy under 808 nm laser irradiation (Fig. 4a). Compared to cells without light exposure, both IR820 and IR820@XOF(Br)-TPy treatment groups showed a significant reduction in cell viability under irradiation. Importantly, IR820@XOF(Br)-TPy exhibited a greater reduction in cell viability at the same IR820 concentration compared to free IR820, indicating that photothermal therapy (PTT) induced by IR820@XOF(Br)-TPy was more effective at eliminating cancer cells. To further visualize the PTT effect, live/dead cell staining was performed using calcein-AM/propidium iodide (PI) after 808 nm irradiation (Fig. 4c). Inverted fluorescence microscope images of the co-stained cells (Fig. 4c) confirmed significant cell death in the IR820@XOF(Br)-TPy treatment group under irradiation. These cells showed weak green fluorescence (live cells) and strong red fluorescence (dead cells), allowing for a clear visual comparison of cell death rates (Fig. 4b). Cells treated with free IR820 also showed

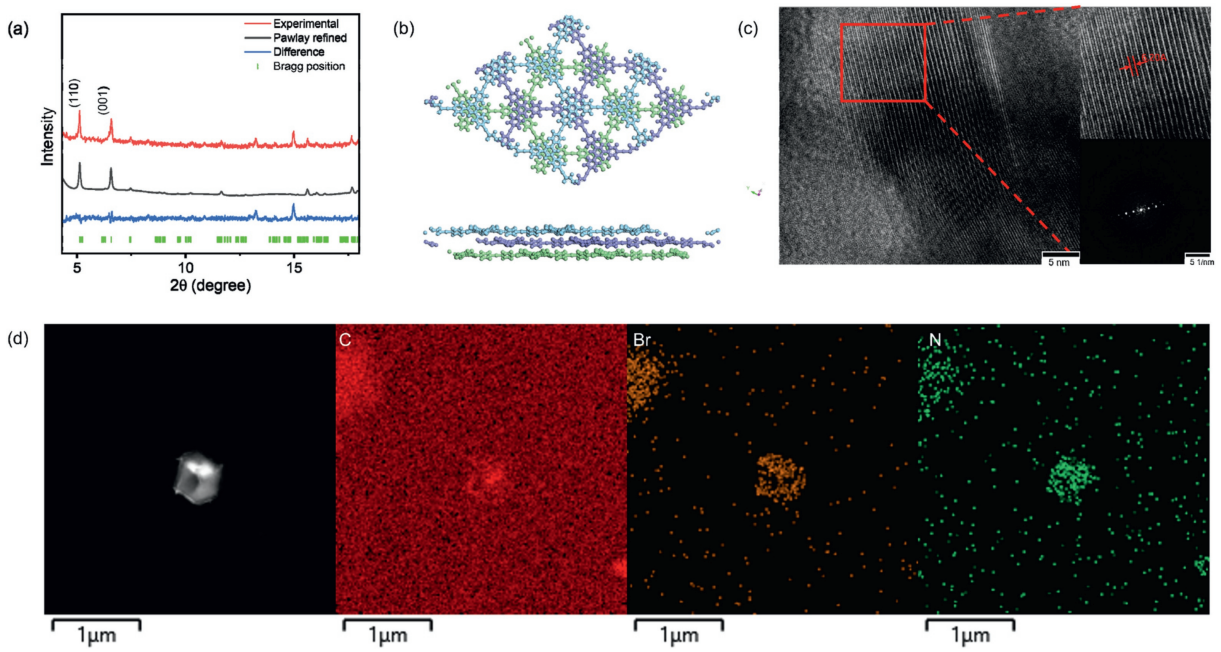



**Fig. 2.** (a) Experimental and refined PXRD, the difference plots between the experimental and refined PXRD patterns, and Bragg positions for XOF(Br)-TPy. (b) The ABC stacking models of XOF(Br)-TPy. (c) HRTEM and SAED images of XOF(Br)-Tpy. (d) EDS-mapping images of XOF(Br)-TPy.

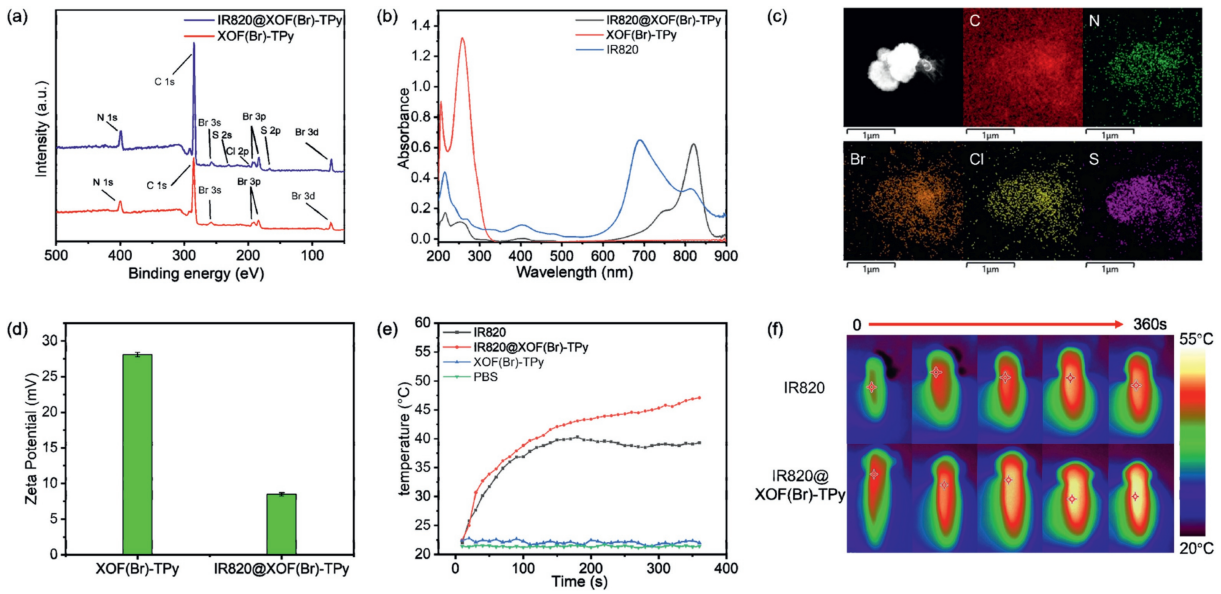



**Fig. 3.** (a) XPS full spectra for XOF(Br)-TPy and IR820@XOF(Br)-TPy. (b) UV–vis absorbance profiles of XOF(Br)-TPy, IR820 and IR820@XOF(Br)-TPy. (c) EDS element mapping of C, N, Br, S and Cl of IR820@XOF(Br)-TPy. (d) Zeta-potential of XOF(Br)-TPy and IR820@XOF(Br)-TPy. (e) Photothermal effect of IR820@XOF(Br)-TPy under 808 nm LED light (0.66 W/cm$^{-2}$) irradiation with IR820, XOF(Br)-TPy and H2O used as control samples. (f) Infrared thermal images of IR820 and IR820@XOF(Br)-TPy under 808 nm LED light irradiation.

some apoptosis, but a larger proportion of live cells remained, consistent with the CCK-8 results.

To evaluate the *in vivo* antitumor effect, a subcutaneous tumor model was established in nude mice using U87 cells. When tumors reached a diameter of 3 mm, mice were randomly divided into four groups: untreated control (NC), XOF(Br)-TPy, IR820, and IR820@XOF(Br)-TPy. Treatments were administered according to the experimental protocol. Based on cytotoxicity assays and previous *in vitro* photothermal studies, it was confirmed that none of the treatments exhibited significant therapeutic effects without 808 nm laser irradiation. Therefore, all *in vivo* tumor experiments were conducted with 808 nm laser irradiation. *In vivo* photothermal experiments were conducted on U87 tumor-bearing mice treated with PBS and IR820@XOF(Br)-TPy (Figs. 5b and c). Under IR820@XOF(Br)-TPy group, 300 s of 808 nm laser irradiation led to a rapid temperature increase at the tumor site from 31 °C to 51 °C, a temperature sufficient to cause irreversible damage to tumor cells. No significant temperature increase was observed in the PBS treatment group.

Tumor volume changes were used to evaluate therapeutic efficacy (Figs. 5d and e). Tumor volume in the untreated group increased rapidly, reaching approximately 22 times the initial volume (Fig. S9 in Supporting information). Both IR820 and IR820@XOF(Br)-TPy effectively reduced the rate of tumor growth.

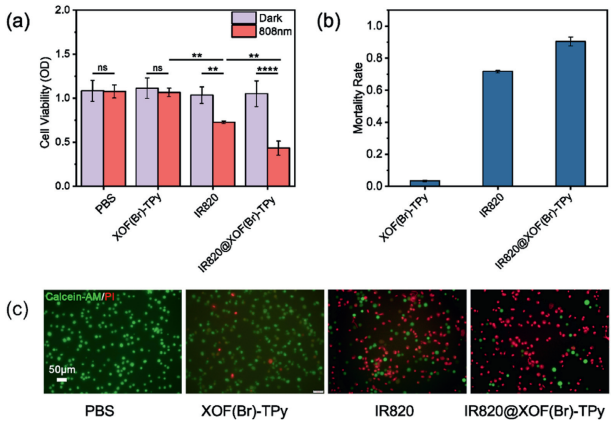



**Fig. 4.** (a) Relative viability of U87 cancer cells after incubation with IR820@XOF(Br)-TPy with or without different light irradiation. Data are presented as means ± SD ($n = 3$); P value was determined by a Student's *t*-test: $^{****}P < 0.0001$. (b) Mortality rate of U87 cancer cells after incubation with IR820@XOF(Br)-TPy under 808 nm laser irradiation. (c) Live/dead staining of U87 cells after different treatments under 808 nm laser irradiation.

Notably, the tumor volume in the IR820@XOF(Br)-TPy group was only 4 times the initial volume, significantly smaller than that of the IR820 group (10 times the initial volume). This difference likely stems from the higher temperature achievable by IR820@XOF(Br)-TPy under light irradiation and the oxidation properties associated with $Br^+$, resulting in stronger tumor cell killing capability compared to IR820, consistent with *in vitro* photothermal results. This confirms that PTT using IR820 loaded onto XOF exhibits significant antitumor efficacy. After 15 days of treatment, no significant body weight fluctuations were observed in the tumor-bearing mice (Fig. 5f), demonstrating good *in vivo* biological safety for IR820@XOF(Br)-TPy. Tumor treatment efficacy was further assessed by hematoxylin and eosin (H&E) staining of tumor sections (Fig. 5g).

H&E staining images revealed varying degrees of damage to tumor cells in the IR820 and IR820@XOF(Br)-TPy groups. Notably, compared to the IR820 group, the IR820@XOF(Br)-TPy group under 808 nm irradiation (right side of the dashed line) exhibited more extensive tumor cell death, demonstrating enhanced therapeutic efficacy and further confirming the superior photothermal performance of IR820@XOF(Br)-TPy. In contrast, tumor cells in the PBS and XOF(Br)-TPy groups maintained intact morphology, indicating

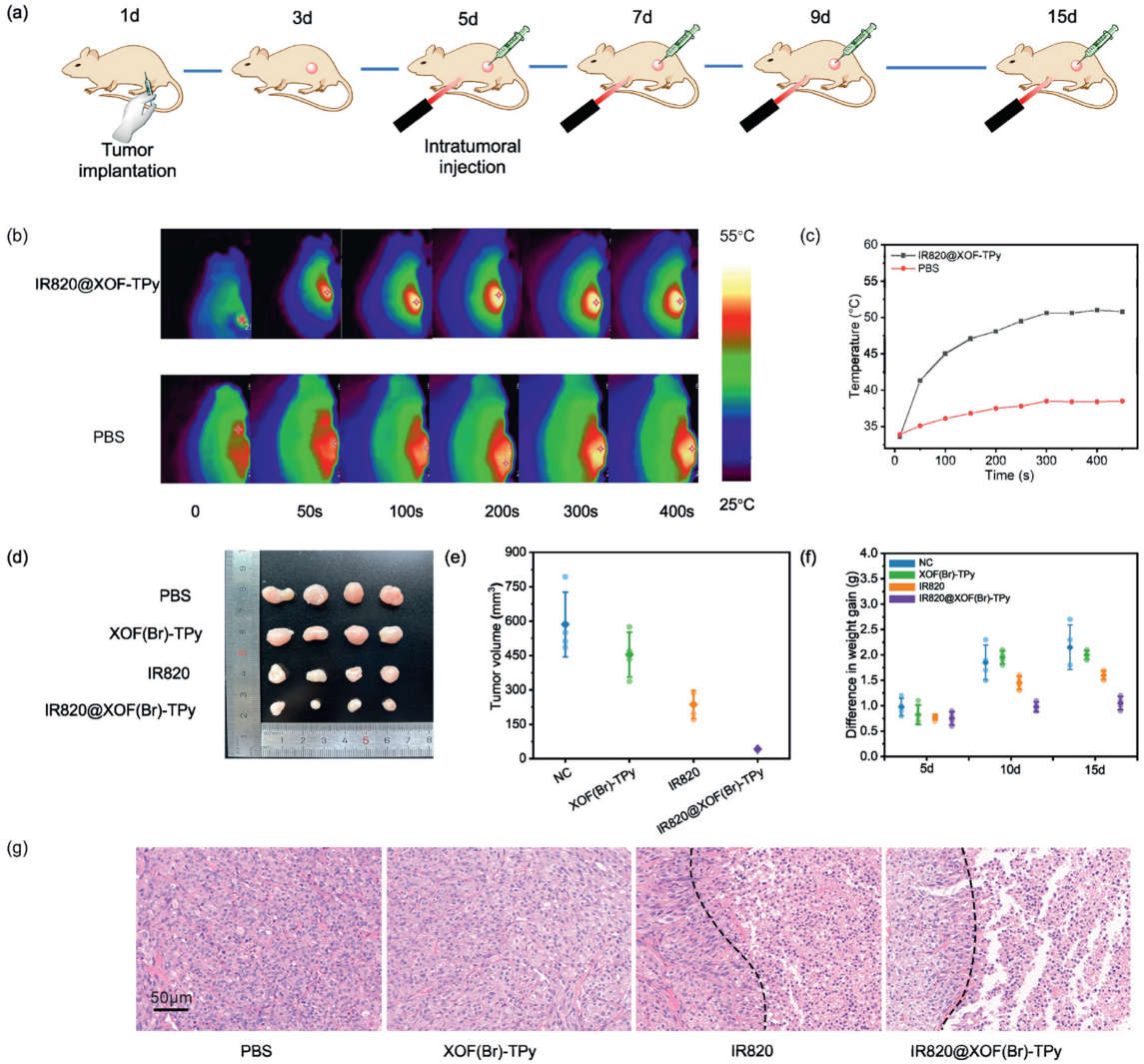



**Fig. 5.** *In vivo* evaluation of IR820@XOF(Br)-TPy-based PTT. (a) *In vivo* antitumor treatment program. (b) Photothermal images and (c) corresponding heating curves of U87 tumor-bearing mice treated with PBS or IR820@XOF(Br)-TPy under 808 nm laser irradiation. (d) Images of the tumors obtained after different treatment. (e) Tumor volume after the therapy. (f) Body weights growth curves of various mice groups under different treatments. (g) H&E-stained sections of tumor tissues subjected to different treatments, respectively.

that 808 nm light alone caused negligible damage to the tumor cells. This suggests that IR820@XOF(Br)-TPy exerts its therapeutic effect exclusively under 808 nm light, highlighting the indispensable synergy between the two components. Organs from all treatment groups exhibited normal cellular morphology after treatment (Fig. S10 in Supporting information).

In conclusion, we have successfully prepared a novel halogen-bonded organic framework, XOF(Br)-TPy, *via* a facile ligand exchange method. Comprehensive spectroscopic characterization, including $^{1}$H NMR, XPS, FT-IR, and PXRD, confirmed the formation of [N···Br$^{+}$···N] halogen bonds and elucidated its crystal structures. The resulting material exhibited good thermal stability. Furthermore, we demonstrated the successful loading of the photothermal agent IR820 onto XOF(Br)-TPy, creating IR820@XOF(Br)-TPy. *In vitro* and *in vivo* studies revealed that IR820@XOF(Br)-TPy, upon 808 nm laser irradiation, exhibited superior photothermal performance compared to free IR820, leading to more effective tumor cell ablation. This work not only indicated that the ligand exchange strategy represents a universal and facile approach for constructing XOFs(Br), but also demonstrated the potential of XOF(Br) as a promising carrier for therapeutic agents in cancer therapy.

## Declaration of competing interest

The authors declare that they have no known competing financial interests or personal relationships that could have appeared to influence the work reported in this paper.

## CRediT authorship contribution statement

**Siyi Lin:** Writing – review & editing, Data curation, Formal analysis, Writing – original draft, Investigation. **Qingxue Xu:** Data curation, Formal analysis, Writing – original draft. **Xuguan Bai:** Data curation, Methodology. **Zhennan Tian:** Methodology. **Lu Wang:** Resources. **Fuxin Han:** Funding acquisition, Methodology, Resources. **Shigui Chen:** Conceptualization, Project administration, Supervision, Writing – review & editing. **Qiang Cai:** Funding acquisition, Validation, Supervision, Writing – review & editing, Resources.

## Acknowledgments

This work was supported by the National Natural Science Foundation of China (Nos. 22371218, 82271518, 21801194), Xianyang Bureau of Science and Technology (No. L2024-QCY-ZYYJJQ-260), The Interdisciplinary Innovative Talents Foundation from Renmin Hospital of Wuhan University (No. JCRCFZ-2022-030), Guiding Projects of Traditional Chinese Medicine in 2023∼2024 by Hubei Provincial Administration of Traditional Chinese Medicine (No. ZY2023F038). We thank the support of the Core Facility of Wuhan University and the Large-scale Instrument and Equipment Sharing Foundation of Wuhan University.

## Supplementary materials

Supplementary material associated with this article can be found, in the online version, at doi:10.1016/j.cclet.2025.111425.

## References

[1] R.L. Siegel, K.D. Miller, H.E. Fuchs, A. Jemal, CA: Cancer J. Clin. 72 (2022) 7–33.
[2] W. Fan, B. Yung, P. Huang, X. Chen, Chem. Rev. 117 (2017) 13566–13638.
[3] D. Peer, J.M. Karp, S. Hong, et al., Nat. Nanotechnol. 2 (2007) 751–760.
[4] X.Q. Mao, J. Xu, W. Wang, et al., Mol. Cancer 20 (2021) 1–30.
[5] L. Zitvogel, L. Apetoh, F. Ghiringhelli, G. Kroemer, Nat. Rev. Immunol. 8 (2008) 59–73.
[6] R. Baskar, K.A. Lee, R. Yeo, K.W. Yeoh, Int. J. Mol. Sci. 9 (2012) 193–199.
[7] W. Ngwa, O.C. Irabor, J.D. Schoenfeld, et al., Nat. Rev. Cancer 18 (2018) 313–322.
[8] H. Nelson, N. Petrelli, A. Carlin, et al., J. Natl. Cancer Inst. 93 (2001) 583–596.
[9] J.W. Lee, J.H. Park, M.R. Prausnitz, Biomaterials 29 (2008) 2113–2124.
[10] E. Larrañeta, R.E.M. Lutton, A.D. Woolfson, R.F. Donnelly, Mater. Sci. Eng. R: Rep. 104 (2016) 1–32.
[11] X. Deng, Z. Shao, Y. Zhao, Adv. Sci. 8 (2021) 2002504.
[12] H.S. Jung, P. Verwilst, A. Sharma, et al., Chem. Soc. Rev. 47 (2018) 2280–2297.
[13] J.J. Huo, Q.Y. Jia, H. Huang, et al., Chem. Soc. Rev. 50 (2021) 8762–8789.
[14] X.H. Huang, I.H. El-Sayed, W. Qian, M.A. El-Sayed, J. Am. Chem. Soc. 128 (2006) 2115–2120.
[15] K. Li, M. Lu, X.H. Xia, Y.Y. Huang, Chin. Chem. Lett. 32 (2021) 1010–1016.
[16] M. Karimi, S. Bahrami, S.B. Ravari, et al., Expert Opin. Drug Deliv. 13 (2016) 1609–1623.
[17] F. Lu, Z. Li, Y. Sheng, et al., Biomaterials 276 (2021) 121035.
[18] M. Karimi, H. Mirshekari, S.M. Moosavi Basri, et al., Adv. Drug. Deliv. Rev. 106 (2016) 45–62.
[19] Y. Rui, S. Wang, P.S. Low, D.H. Thompson, J. Am. Chem. Soc. 120 (1998) 11213–11218.
[20] X. Yi, J.-J. Hu, J. Dai, et al., ACS Nano 15 (2021) 3026–3037.
[21] X. Peng, Q. Pan, B. Zhang, et al., Biomacromolecules 20 (2019) 2372–2383.
[22] Y. Yin, P. Zeng, Y. Duan, et al., J. Mater. Chem. B 12 (2024) 8099–8106.
[23] Y. Yin, P. Sun, H. Dong, et al., Chin. Chem. Lett. 34 (2023) 108594.
[24] E. de las Heras, M.L. Sagristá, M. Agut, S. Nonell, Pharmaceutics 14 (2022) 405.
[25] J.F. Han, Q. Wang, Z.R. Zhang, et al., Small 10 (2014) 524–535.
[26] D.Y. Xia, P. Wang, X.F. Ji, et al., Chem. Rev. 120 (2020) 6070–6123.
[27] Z.C. Liu, S.K.M. Nalluri, J.F. Stoddart, Chem. Soc. Rev. 46 (2017) 2459–2478.
[28] K. Ariga, M. Nishikawa, T. Mori, et al., Sci. Technol. Adv. Mater. 20 (2019) 51–95.
[29] J.R. Wu, G.X. Wu, D.X. Li, Y.W. Yang, Angew. Chem. Int. Ed. 135 (2023) e202218142.
[30] B. Hazarika, V.P. Singh, Chin. Chem. Lett. 34 (2023) 108220.
[31] C. Yin, Z.-A. Yan, R. Yan, et al., Adv. Funct. Mater. 34 (2024) 2316008.
[32] J. Li, C. Yang, H.Z. Li, et al., Adv. Mater. 18 (2006) 2969–2974.
[33] Y. He, J. Wang, S. Wang, et al., Nano Today 48 (2023) 101700.
[34] P. Metrangolo, G. Resnati, T. Pilati, S. Biella, Halogen bonding in crystal engineering, in: P. Metrangolo, G. Resnati (Eds.), Halogen Bonding: Fundamentals and Applications, Berlin, 2008, pp. 105–136.
[35] M.H. Kolář, P. Hobza, Chem. Rev. 116 (2016) 5155–5187.
[36] G.R. Desiraju, P.S. Ho, L. Kloo, et al., Pure Appl. Chem. 85 (2013) 1711–1713.
[37] L. Turunen, M. Erdélyi, Chem. Soc. Rev. 49 (2020) 2688–2700.
[38] A. Karim, M. Reitti, A.C.C. Carlsson, et al., Chem. Sci. 5 (2014) 3226–3233.
[39] J.L. Dutton, Chem. Sci. 14 (2023) 3961–3962.
[40] S.L. Yu, J.S. Ward, K.N. Truong, K. Rissanen, Angew. Chem. Int. Ed. 60 (2021) 20739–20743.
[41] L. Turunen, A. Peuronen, S. Forsblom, et al., Chem. Eur. J. 23 (2017) 11714–11718.
[42] U. Warzok, M. Marianski, W. Hoffmann, et al., Chem. Sci. 9 (2018) 8343–8351.
[43] S. Yu, E. Kalenius, A. Frontera, K. Rissanen, Chem. Commun. 57 (2021) 12464–12467.
[44] A. Vanderkooy, A.K. Gupta, T. Földes, et al., Angew. Chem. Int. Ed. 58 (2019) 9012–9016.
[45] M.P. Moghadasnia, B.J. Eckstein, H.R. Martin, et al., Cryst. Growth Des. 24 (2024) 2304–2321.
[46] J.N. Smith, C.I. Hunter, H.V. Doan, et al., Angew. Chem. Int. Ed. 64 (2025) e202422197.
[47] Z. Tian, J. Zhao, G. Gong, et al., Sci. Sin. Chim. 53 (2023) 2367–2377.
[48] G.F. Gong, S.H. Lv, J.X. Han, et al., Angew. Chem. Int. Ed. 60 (2021) 14831–14835.
[49] S. Wang, H. Dong, G. Gong, et al., Mater. Chem. Front. 8 (2024) 4096–4105.
[50] Q. Zhao, P. Sun, G. Gong, et al., Sci. China Chem. 68 (2025) 631–640.
[51] S. Maji, R. Natarajan, Small 19 (2023) 2302902.
[52] J. Zhao, N. Xia, Z. Tian, et al., ACS Mater. Lett. 6 (2024) 508–516.
[53] X. Bai, Z. Tian, H. Dong, et al., Angew. Chem. Int. Ed. 63 (2024) e202408428.
[54] P. Sun, H. Dong, S. Lv, et al., J. Mater. Chem. A 12 (2024) 1128–1134.
[55] N. Xia, J. Han, F. Xie, et al., ACS Appl. Mater. Interfaces 14 (2022) 43621–43627.
[56] H.Q. Dong, S.B. Yu, S.-M. Wang, et al., Chin. Chem. Lett. 36 (2025) 110730.
[57] Z. Tian, S. Zhou, Y. Qu, et al., Aggregate 6 (2025) e70050.
[58] Q. Zhao, S. Lin, P. Sun, et al., Adv. Funct. Mater. 35 (2025) 2421755.